Insights into spatiotemporal dynamics of riverine water age and its controlling factors in five contrasting subtropical headwater catchments, South-Central China using stable water isotopes

Kaiwen Li[1,2], Huawu Wu[1,2], Jing Li[3], Mengyao Ding [2,4], Ruiyu Lei [2,4], Lihui Tian [5], Hongxiang Fan [2], Congsheng Fu [2], Rongrong Wan [2], and Guishan Yang [1,2]

[1]The National Key Laboratory of Water Disaster Prevention, Hohai University, Nanjing, China.
[2]Key Laboratory of Lake and Watershed Science for Water Security, Nanjing Institute of Geography and Limnology, Chinese Academy of Sciences, Nanjing, China.
[3]Geographic Information and Tourism College, Chuzhou University, Chuzhou, China
[4]University of Chinese Academy of Sciences, Beijing, China.
[5]State Key Laboratory of Plateau Ecology and Agriculture, Qinghai University, Xi'ning, China.

Correspondence: Huawu Wu (wuhuawu416@163.com)

Abstract. Understanding river water age and its controlling factors are fundamental for comprehending catchment hydrological and biogeochemical processes. However, how do landscape characteristics and climate properties control the spatiotemporal heterogeneity of riverine water age remain to be further clarified in subtropical headwater catchments. This study used stable isotopic ratios (δD and $\delta^{18}O$) from five contrasting headwater catchments. The study explored time-variable young (F_{yw}) and

5   new (F_{new}) water fraction among five contrasting headwater catchments from the upper reaches of Xiu River, located within the Poyang Lake catchment of South-Central China using stable isotopes (δD and $\delta^{18}O$) from 2021 to 2023. The isotopic compositions of precipitation exhibited greater fluctuations than those of river water from five sub-catchments. The lower slopes (3.78 to 6.63) and intercepts (-13.12 to 2.65) of linear regression correlations between δD and $\delta^{18}O$ were observed in river water compared to the global and local meteoric water lines, indicating significant evaporation effects on river water. The young

10   water fraction (F_{yw}) showed considerable spatial variability ranging from 0.07 to 0.21 among five sub-catchments, suggesting the dominant recharge of groundwater to the river. The pronounced temporal variations of F_{yw} highlighted its susceptibility to short-term hydroclimatic change. Random forest models revealed that precipitation ($25.48\pm5.41\%$) and potential evapotranspiration ($27.84\pm6.62\%$) were the primary drivers for young and new water generation. Furthermore, F_{yw} was significantly influenced by upstream inflows ($24.21\pm0.71\%$), whereas F_{new} was more susceptible to the influence of percentage of forest

15   (22.63%) and cropland (29.85%). Shapley Additive Explanations reveal a significant negative correlation between river area and F_{yw}, and a significant positive correlation between agricultural area proportion and F_{new}. Combined with the dynamic variations in the F_{yw} and F_{new}, these results indicated that the regulatory function of riparian zones played a crucial role in young water generation, while land use changes significantly altered the process of new water generation. Our findings suggest that intensified evapotranspiration and increased precipitation will significantly impact the generation of riverine young and new

20   water in the context of global warming and land use type changes.

1 Introduction

Stable isotopes (δ^{18}O and δD) have been widely used as ideal tracers to elucidate different sources of stream flow, assess the variability of this source partitioning with precipitation characteristics, and evaluate the origin and age of river water (Ide et al., 2020; Morissette et al., 2023; Valdivielso et al., 2020). Water age serves as a valuable descriptor of specify storage, routes, and differential source waters within catchments, bearing significant implications for the management of water resources in terms of both quantity and quality (Benettin et al., 2020). Mean transit time (MTT) and young water fraction (F_{yw}, the proportion of water younger than two or three months) are two crucial water age metrics, that have been extensively employed in hydrological researches (Jasechko et al., 2016; Speed et al., 2011; Xiao et al., 2021). These metrics integrate flow path heterogeneity and directly relates to internal catchment processes, which differs in each catchment depending on the landscape, climatic parameters and human activities within each catchment. Furthermore, Kirchner(2019) proposed a method using a modified mixing model to estimate the new water fraction (F_{new}, the proportion of water younger than one or two weeks,Kirchner, 2019). When used together, F_{yw} and F_{new} offer complementary methods for estimating water origins and different flow paths (Burt et al., 2023). Although several studies have investigated the relationships between catchment topography and water age (Clow et al., 2018; Jasechko et al., 2016), few have expanded the analysis to encompass a wide range of controlling factors and assessed the influence of the selected calculation methods. Given the paucity of such studies, there is a need for a more comprehensive appraisal the relationships between landscape and hydro-climatic factors with water age metrics through nested catchment investigations.

F_{yw} is defined as the fraction of streamflow younger than a specified threshold and is used to quantify the proportion of precipitation input that is rapidly converted into runoff as fast flow (Kirchner, 2016). This metric is independent of old water components and is negligibly affected by aggregation bias compared to MTT (Kirchner, 2016). Therefore, F_{yw} is increasingly used to study hydrological processes in highly heterogeneous catchments. Substantial research efforts have focused on elucidating the relationships between F_{yw} and intrinsic catchment characteristics such as topographic metrics (Jasechko et al., 2016), geology (Wang et al., 2023), and soil characteristics (Ye et al., 2022) to identify potential controlling factors. For example, several studies have found that high-gradient or high-elevation catchments tend to exhibit lower F_{yw} values (Jasechko et al., 2016; Song et al., 2017), whereas other studies have reported the opposite relationship (Clow et al., 2018; Zhang et al., 2018). Hence, F_{yw} is characterized by highly spatial heterogeneity and complex controlling factors, constraining the understanding of catchment hydrological processes. Furthermore, studies have emphasized that the distribution of fast and slow flow paths is subject to temporal variability (Harman, 2015; Kim et al., 2016), suggesting that the characteristics of river water age can change over time. von Freyberg et al (2018) utilized flow-weighted fits of seasonal tracer cycles to predict the flow-weighted average young water fraction (F^{*}_{yw}, compared to the unweighted F_{yw}) (von Freyberg et al., 2018). Their study illustrated dynamic temporal variability in F_{yw} within sites but found no clear relationship between catchment gradient and F^{*}_{yw}. Generally, when examining the effects of hydroclimatic variables (e.g., precipitation and evapotranspiration) and landscape characteristics (e.g., elevation) on F_{yw}, single-variable correlations should be interpreted with caution, as they may be confounded by cross-correlations among

many potential drivers(Lutz et al., 2018). Thus, it remains unclear that which of these variables exert a first-order control on
F_{yw} in subtropical catchments with highly variable precipitation and complex landscapes properties.

As the largest freshwater lake in China, Poyang Lake is dominated by a typically subtropical climate and serves as a
crucial floodwater storage area for the Yangtze River. Hence, it plays a vital role in the management and ecological conser-
vation of the Yangtze River Catchment. The intricate hydrological exchanges between the lake, its five tributary rivers, and
the Yangtze River leads to significant intra-annual variations in the water level of Poyang Lake, driven by highly precipitation
variability. In recent years, significant changes in the hydrological characteristics of Poyang Lake have occurred due to the
combined effects of natural factors and human activities. These changes are marked by earlier onset of dry seasons, rapid
declines in water levels during autumn and winter, prolonged dry spells, and consistently low water levels. For example, in
2022, a severe drought caused an unusual phenomenon of low water levels during the flood season (Guan et al., 2022). The
complex hydrological regime necessitates a thorough understanding of the origins of streamflow in the headwater catchment
and their potential changes under future climates. However, this complexity also poses challenges for numerical simulations
and traditional hydrological monitoring methods in depicting these hydrological processes. Thus, it is necessary to employ
isotope techniques to analyze these processes. Current isotope analysis in Poyang Lake catchment have primarily focused on
groundwater recharge within the catchment (Mao et al., 2021) and the interaction between Poyang Lake and the Yangtze River
(Wu et al., 2021). However, limited research has been conducted on the transportation and storage dynamics of headwater
rivers that feed into lakes. Specifically, there is a need to understand the proportion of streamflow originating from old water
stored in subsurface layers versus new water derived from recent precipitation. It likewise remains unclear how these slow and
fast flow processes, and thus the partitioning of old and new water in headwater streams, relate to hydroclimatic forcing and
physical catchment characteristics.

To address the aforementioned knowledge gaps, this study conducted continuous observations of precipitation and river
water isotopes over two years in five contrasting headwater catchments from the upper reaches of Xiu River, located in Poyang
Lake Catchment, South-Central China. We explored the seasonal isotope cycles of water components in the catchment and used
an array of potential drivers of riverine water age metrics to achieve the following objectives: 1) examine the characteristics
of stable isotopes among fiver contrasting sub-catchments; 2) compare water age metrics across different catchments using
different calculation methods; 3) identify the relative importance of different factors controlling young and new water fraction.

2 Materials and methods

2.1 Study area

Poyang Lake Catchment, covering the entire Jiangxi Province in South-Central China, is connected to the mid- and
lower reaches of the Yangtze River (Figure 1). This region is dominated by a subtropical humid monsoon climate with mild
temperatures, abundant rainfall, ample sunlight, and a prolonged frost-free period. The four seasons are distinct, with cold and
dry winters, and summers influenced by the subtropical anticyclone, characterized by hot and sunny weather with occasional
typhoon impacts. The average annual rainfall is 1655.9 mm, which is unevenly distributed throughout the seasons and mainly

concentrated during the flood season (April to September), accounting for 60-70% of the annual rainfall. Influenced by inflows from the "Five rivers" (e.g., Gan River, Fu River, Xin River, Rao River, and Xiu River), Poyang Lake is characterized by a typical water conveyance-type lake, which is connected to large river systems that subsequently flow into the Yangtze River after being regulated and stored (Li et al., 2016). During high water-level periods, Poyang Lake exhibits lake-like characteristics from April to September, while it resembles a river during low water-level periods from December to January (Wu et al., 2021). Furthermore, the temporal and spatial distribution of precipitation throughout the year has become increasingly uneven. Particularly since June 2022, the region has witnessed the most intense heatwave event in terms of overall intensity since complete observational records began in 1961(Guan et al., 2022).
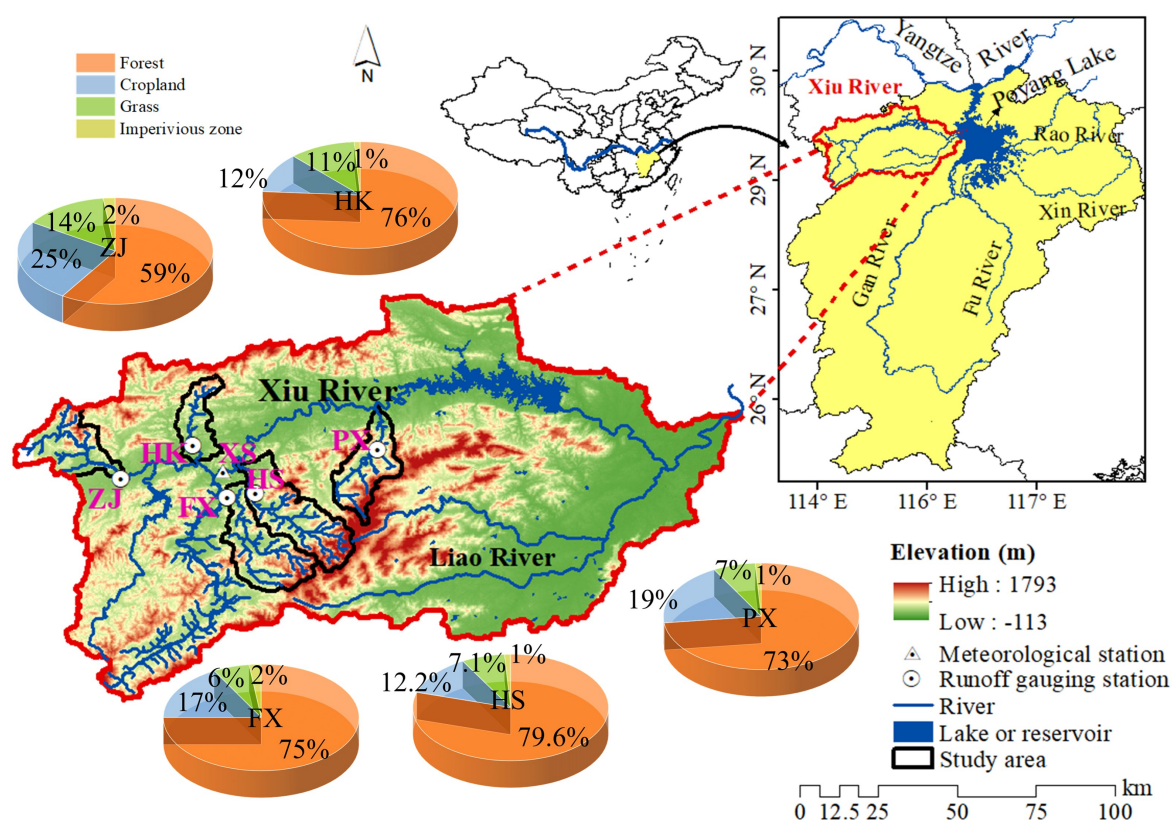
Figure 1. Geographical location and catchment properties (e.g., topography and land use) of the study area

The Xiu River catchment is located in the western part of Poyang Lake, covering area of 14,797 km² with 8.3 % of the total area of Poyang Lake catchment (Figure 1). The five sub-catchments of HS, PX, ZJ, HK, and FX within Xiu River catchment represent the Huangsha, Panxi, Zhajin, Hangkou, and Fengxiang catchments, respectively, spanning from 281.22 km² to 662.25 km². Geomorphological and hydrological characteristics of the study sites are reported in Table 1. During the study period, the multi-year average rainfall of 1638.4 mm/year, of which 55 % is occupied in March to June. The mean annual

100 evapotranspiration is 1049 mm/year, with peak rates occurring during May and September. The water year was separated into four hydrologically contrasting seasons: spring (March-May), summer (June-August), autumn (September-November) and winter (December-February). The primary land use type in the study area is forest (Figure 1). This is followed by cropland, with smaller areas for grassland, urban centers, and open water bodies. The proportion of forested area within the catchment varies from 59 % to 79.6 %. Huangsha catchment (HS) shows the highest proportion of forest cover whereas Zhajin catchment

105 (ZJ) exhibits the lowest proportion of forested area (Figure 1). Regarding soil type, red soil dominates at 24 %, accompanied by paddy soil at 7.1 % and yellow soil at 7.2 %.

Table 1. Detailed information of the sampling sites and catchment properties.

Station	Catchment	Lon(°)	Lat(°)	Area(km^2)	Flow length(km)	TWI	Slope(°)	Drainage density(km/km^2)
Luoxi	Panxi River(PX)	114.9	29.1	329.5	48.3	6.3	17.4	0.4
Chaiduan	Hangkou River(HK)	114.4	29.1	281.2	37.6	6.6	15.5	0.2
Zhajin	Zhajin River(ZJ)	114.3	29	488.4	44.3	6.0	14.1	0.3
Chijiang	Fengxiang River(FX)	114.6	28.9	586.2	56	6.7	17.2	0.3
Huangsha	Huangsha River(HS)	114.6	28.9	662.3	7.1	6.3	18.3	0.3

Notes: TWI (Topographic Wetness Index), represents the influence of land elevation on the direction and accumulation of runoff. It is calculated using the formula: TWI=ln(A/tanβ), where A is the specific catchment area (drainage area per unit contour length), and β is the slope of the terrain derived from the digital elevation model (DEM).

2.2 Water sampling and other date sources

Isotopic sampling campaigns were conducted over two hydrological years (December 2021–December 2023). A total of five river water sampling points were performed in the study area (Figure 1), which was entrusted to the staff of hydrological

110 gauging stations in the study area (Luoxi, Chaiduan, Zhajin, Chijiang, and Huangsha, Table 1). Weekly grab samples for δ^{18}O and δD were collected with a total of 85–109 samples at each site. Samples were collected with a 1-L stainless steel sampler dipped in the middle of the current flow at depths below 15 cm. All bottles were fully filled and then transferred to clean and dry 50-mL polyethylene bottles, which were sealed immediately and stored in refrigerator to avoid isotopic fractionation prior to analysis. In addition, daily precipitation amounts were recorded by Xiushui County meteorological station (XS, Figure 1),

115 268 event-based precipitation samples were collected from November 2021 to December 2023. Each sample was collected as soon as a precipitation event stopped to reduce evaporation.

Stable isotopes (δ^{18}O and δD) of all water samples were measured by a Laser Absorption Water-Vapor Isotope Spectrometer (Model 908-0004, Los Gatos Research, Mountain View, CA, USA) in the State Laboratory of Nanjing Institute of Geography and Limnology, Chinese Academy of Sciences. Measured results are reported as δ^{18}O and δD in ‰ relative to

120 the Vienna Standard Mean Ocean Water (VSMOW). Isotopic ratios (δD and δ^{18}O) are expressed using the conventional delta notation (δ): δsample = (Rsample / RV-SMOW - 1) × 1000‰, where Rsample and RV-SMOW are the isotope ratios (^{2}H / ^{1}H, ^{18}O / ^{16}O) of water samples and V-SMOW, respectively. The precision of the isotopic analysis is ± 0.2‰ for δ^{18}O and

± 0.6‰ for δD. Lastly, d-excess (d-excess=δD-8δ¹⁸O) of the precipitation and river water was calculated using the slope and intercept of the global meteoric water line, as an important indicator of the difference in kinetic fractionation, which results

125   from different diffusivities of water isotopes during water phase changes(Bagheri et al., 2019).

We used the HydroATLAS database to extract hydrological attributes of the catchment, including soil water content (SWC), groundwater table depth (GTD), river volume (RV), stream gradient (SG), river area (RA), the Climate Moisture Index (CMI), and the Global Aridity Index (GAI), among others. Additionally, potential evapotranspiration (PET) was calculated using the Penman equation. Soil type data were sourced from the HWED global soil database, developed by FAO and IIASA.

130   Land use data for the 2020 were obtained from the National Land Cover dataset provided by the Institute of Remote Sensing and Digital Earth, Chinese Academy of Sciences, with a spatial resolution of 30m. The DEM data used is SRTM30, jointly measured by the National Imaging and Mapping Agency (NIMA) of the U.S. Department of Defense and NASA, with a spatial resolution of 30m. Flow Length was calculated as the distance along the flow path from each point in the catchment to the outlet. This was determined using the DEM to derive the flow direction, which was then used to trace the flow path and

135   compute the cumulative length of the flow lines.

2.3   Young water fraction (F_{yw}) estimation

This study employed the sine-wave method to estimate F_{yw}, following the methodology outlined by Kirchner (2016). Specifically, we will use the termed F_{yw_all} to denote F_{yw} derived from utilizing a single sine wave for the entire 2-year time series of precipitation and streamflow isotope data. The amplitude and phase shift of seasonal cycles in water isotopes offer

140   an objective representation of the inputoutput dynamics within catchments. This approach assumes that the seasonal isotope pattern in precipitation is mirrored in river water with a damped and delayed signal. The mathematical expression for the sine-wave approach describing the seasonal cycles of river water and precipitation isotopes is as follows:

$$Cp(t) = ap\cos(2\pi ft) + bp\sin(2\pi ft) + kp \tag{1}$$

$$Cs(t) = as\cos(2\pi ft) + bs\sin(2\pi ft) + ks \tag{2}$$

145   In the equation provided, the subscripts "s" and "p" correspond to river water and precipitation, respectively. $C_P(t)$ and $C_S(t)$ are the δD of the precipitation and streamflow, respectively. f indicates the frequency of the cycle (f = 1 for a seasonal cycle); t signifies time (years with decimal fractions), utilized as an independent variable for fitting isotopic seasonal fluctuations; the sine curves of Eq.(1) and (2) are fitted on the isotope measurements using the iteratively re-weighted least squares(IRLS) method (for reducing the influence of outliers), which leads to estimates of A, ϕ and k parameters (k is the vertical offset of the

150   seasonal isotope cycle), and a_p, b_p, a_s, b_s are coefficients for determining the amplitude (A) and phase shift (ϕ) of the seasonal δD of precipitation and streamflow, which are calculated as follows:

$$Ap = \sqrt{a_p^2 + b_p^2}, As = \sqrt{a_s^2 + b_s^2} \tag{3}$$

$$\phi_p = \tan^{-1}(\frac{ap}{bp}), \phi_s = \tan^{-1}(\frac{as}{bs}) \tag{4}$$

Here, α represents a shape factor in the transit-time distribution equation, which can be derived from the phase shift and
amplitude ratio between precipitation and streamflow. By successively solving the relationship between the gamma distribution
parameters (α and β) and the amplitude ratio A_s / A_p as well as the phase shift $\phi_p - \phi_p$, the values for α and β can be determined
using Eqs. (5)-(7) (Kirchner, 2016):

$$\phi_s - \phi_p = \alpha \tan^{-1} \sqrt{2\pi f \beta} \tag{5}$$

$$\frac{As}{Ap} = (1 + (2\pi f \beta)^2)^{-\frac{\alpha}{2}} \tag{6}$$

$$\beta = \frac{1}{2\pi f} \sqrt{(\frac{As}{Ap})^{-\frac{\alpha}{2}}} \tag{7}$$

The threshold age (τ_{yw}) of F_{yw} can be calculated using the shape parameter α as follows (Kirchner, 2016a):

$$\tau_{yw} = 0. - 949 + 0.1065\alpha - 0.0126\alpha^2 (R^2 = 0.9998) \tag{8}$$

Kirchner (2016) designed the F_{yw} as the proportion of the transit time distribution younger than a threshold age (τ_{yw}). By
assuming that the transit time distribution mathematical form is the regularized lower incomplete gamma function for all the
study catchments, the theoretical F_{yw} can be expressed as:

$$F_{yw} = \Gamma(\tau, \alpha, \beta) = \int\limits_{t=0}^{t_{yw}} \frac{\tau^{\alpha-1}}{\beta^\alpha \Gamma(\alpha)} e^{-\tau} dt \tag{9}$$

To account for the temporal heterogeneity of F_{yw}, this study uses a 1-year calculation window that was shifted in 1-month
intervals to obtain 60 estimations of individual time-variable F_{yw} result (F_{yw_60} represent the results). A minimum time-window
length of 1 year was chosen to fully capture the annual isotope signal. Due to significant interannual variations in precipitation
and corresponding fluctuations in streamflow, where high flows are associated with more young water and low flows with
baseflow, it is reasonable to use discharge as a representative of catchment wetness to calculate flow-weighted Fyw within each
time window (Gentile et al., 2023). Hereafter, we will use the symbol "$_*$" for referring to a flow-weighted variable, in order to
be consistent with previous studies (Gallart et al., 2020; von Freyberg et al., 2018), to distinguish it from unweighted young
water fraction (F_{yw}). Fitting sine curves using Eq. (2) involved employing an iteratively reweighted least squares algorithm,
with precipitation and runoff volumes serving as weights. Depending on whether the fit is unweighted or flow-weighted, one
can obtain either an unweighted amplitude (A_S) or a flow-weighted amplitude (A^*_S), respectively. Such amplitudes can be
used to calculate the unweighted (Eq.10) or the flow-weighted (Eq.11) young water fractions (F_{yw} or F^*_{yw}, respectively) via
the "amplitude ratio approach":

$$F_{yw} = \frac{As}{Ap} \tag{10}$$

$$F^*_{yw} = \frac{A^*s}{A^*p} \approx \frac{\sum_{i=1}^{n} Q(t_i) F_{yw}(t_i)}{\sum_{i=1}^{n} Q(t_i)} \tag{11}$$

Additionally, $F^*_{yw\_60}$ will represent the 60 individual flow-weighted F_{yw} results using a 1-year calculation window that was
shifted in 1-month intervals. The sine curves of Eqs. (1)-(2) are fitted on the isotope measurements using the IRLS method,

which leads to estimate the mean and standard deviation of A, ϕ and k parameters. Additionally, we estimate the uncertainty of F_{yw}, α, and τ_{yw} assuming all the fitted parameters having a Gaussian distribution with a standard deviation equal to regression

185   error and we generate 1000 random samples of such parameters, and we estimate the optimal F_{yw}, α, and τ_{yw} for each parameter set and then compute their standard deviation.

2.4   New water fraction (F_{new}) estimation

To calculate the new water fraction—the fraction of river water comprised of precipitation that has fallen since the previous sampling (Kirchner, 2019)—we applied an ensemble hydrograph separation framework to the river water δD datasets. In our

190   study, the average time interval between samples was seven days for riverine waters. Thus, the new water fractions represent the proportion of precipitation within each water pool or flux that fell during the preceding approximately one-week period (e.g. < 1 weeks). However, due to the mixing of the isotopic composition of groundwater and the evaporative fractionation that causes deviations from local precipitation isotopes, there may not be significant differences in river water isotopes before and after precipitation, which could render the mixing model applications unfeasible and thus lead to equivocal inferences about

195   recharge origin (Murad and Mirghni, 2011). Consequently, the d-excess value was used to calculate Fnew, which is interpreted as an indicator of non-equilibrium in the straightforward condensation-evaporation process (Craig, 1961). To determine these new water fractions, we first calculated:

$$X_{p,j} - X_{r,j-1} \tag{12}$$

where $X_{p,j}$ represent deuterium isotope composition or deuterium-excess of precipitation at a given sampling time point j, while

200     $X_{r,j-1}$ represent deuterium isotope composition or deuterium-excess of river water at previous sampling time point, j-1. We then calculated:

$$X_{r,j} - X_{r,j-1} \tag{13}$$

where $X_{r,j}$ represent deuterium isotope composition or deuterium-excess of river water at a given sampling time point j. We calculated Eq. (12) and (13) for all river water sampling time points and generated a scatterplot with the results of Eq. (12) on

205   the x-axis and Eq. (13) on the y-axis. The new water fraction is represented by the slope of the regression line between x and y. Finally, we conducted an analysis of Pearson's r to assess the relationship between x and y. As F_{new} can be calculated for different subsets of data like F_{yw}, this study uses a 1-year calculation window that was shifted in 1-month intervals to obtain 60 estimations of individual time-variable F_{new} result (F_{new_60}).

2.5   Machine learning models for identifying driving factors

210   To investigate the importance of the 20 most frequently used controlling factors from previous studies (Jasechko et al., 2016; Song et al., 2017; von Freyberg et al., 2018), including landscape and hydroclimatic factors, in the generation of young and new water, we performed a random forest (RF) analysis. This analysis identified the key factors that significantly affect $F^{*}_{yw\_60}$, F_{yw_60}, and F_{new_60}. The 'rfPermute' package was used to conduct this analysis (Shi et al., 2023). Random forest is

a non-parametric machine learning algorithm that assesses a combination of predictors. Each tree in the forest depends on the values of a random vector sampled independently, with the same distribution for all trees. The generalization error of a random forest depends on the strength of the individual regression trees and converges to a limit as the number of trees in the forest increases (Erdélyi et al., 2023). The forest's predictions are based on the average results of the decision trees, which use bootstrap sampling to reduce the possibility of overfitting (Cotton et al., 2018; Lutz et al., 2018).

Subsequently, this study uses Shapley Additive Explanations (SHAP), a game-theory-based method, to explain the predictive results of RF models and quantify the contribution of driving factors to the model output. Proposed by Lundberg and Lee, SHAP provides both global and local interpretability by evaluating each feature's marginal contribution to the model prediction. Based on Shapley values from cooperative game theory, SHAP measures a feature's contribution by averaging its marginal impact across all possible feature combinations. The formula for calculating SHAP values is as follows:

$$\phi_i(f,x) = \sum_{S \subseteq F\{i\}} \frac{|S|!(k-|S|-1)!}{k!}(f_x(S \cup \{i\}) - f_x(S)) \tag{14}$$

Where ϕ_i (f,x) can be interpreted as the impact of the i-th factor on the prediction of the model, when given an input x. k is the number of factors influencing the model, F is the full feature set, S is a subset of features, and f_x (S) denotes the model prediction for subset S. SHAP's consistency and additive properties make it ideal for disentangling complex, non-linear relationships in environmental data. We computed SHAP (SHapley Additive exPlanations) values using the shapviz package in R to quantify the contribution of each driving factor.

3 Results

3.1 Isotopic and hydrometric data

During the entire study period, the annual average temperature was 18.31°C, with August reaching a peak of 34°C and December recording the lowest temperature at -0.8°C. Temperature and relative humidity exhibited strong seasonal variations, displaying a remarkable anti-phase pattern (Figure A1). Moreover, temporal variations in daily precipitation, the discharge of five sub-catchments in Xiu River catchment are illustrated in Figure 2. Precipitation events primarily occurred between April and June, coinciding with the period of heaviest precipitation (>20 mm). The highest precipitation of 86.1 mm was observed on April 3, 2023, while the total annual rainfall was 1181.88mm in 2022. There was a slight increase in 2023 with an accumulated rainfall of 1314.41 mm. The discharge at four sub-catchments exhibits similar trends with precipitation fluctuation (Figure 2 c-f). These trends include higher discharge in spring and summer, contrasting with lower discharge in winter and autumn. Additionally, the discharge is highest at ZJ among four sub-catchments.

Both precipitation δD and δ^{18}O exhibited significant fluctuations over the observed periods (Figure 2a). δD ranged from -121.39 ‰ to 25.11 ‰ with an amount-weighted average of -34.57‰, while δ18O ranged from -16.78 ‰ to 2.91 ‰, with an amount-weighted average of -6.19‰. In contrast, δ^{18}O and δD values in river water (δ^{18}O: -9.35 to -4.36‰ and δD: -66.43 to -17.22‰) presented smaller variability over time compared with those in precipitation (Figure 3). From a seasonal perspective,
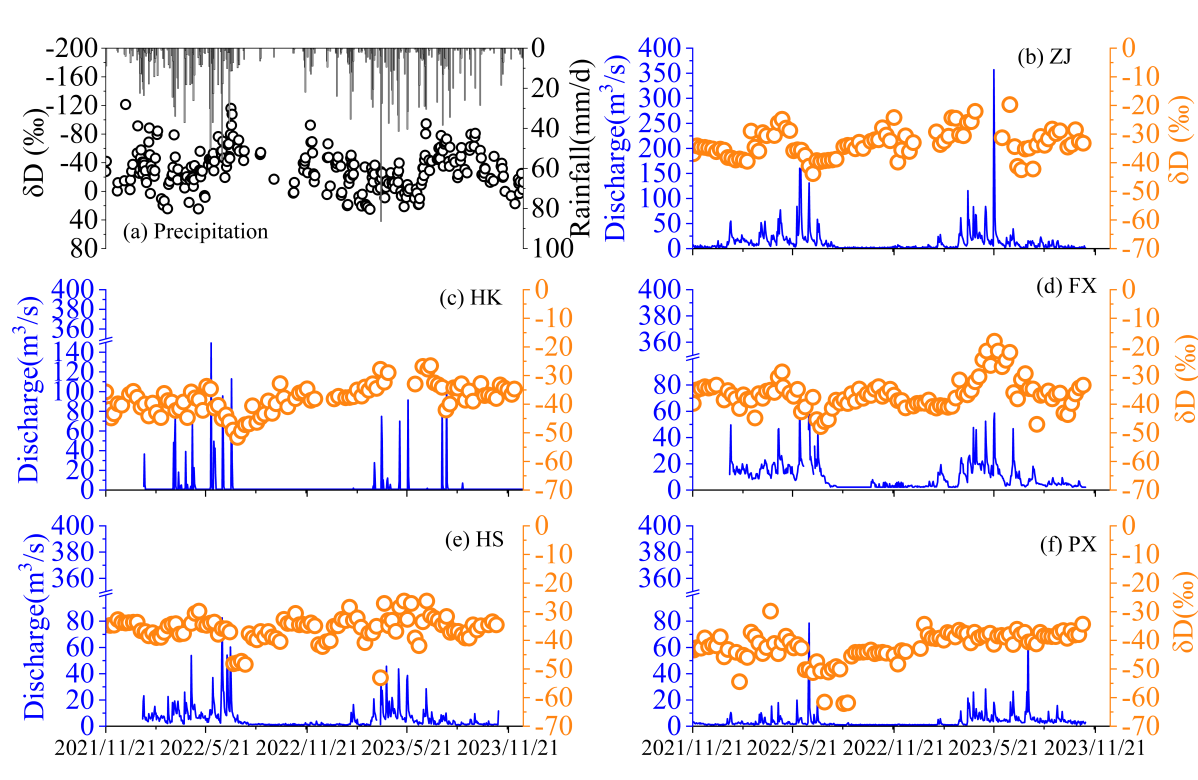
Figure 2. Time series of precipitation amount and precipitation δD (a), discharge and river water δD (b f) from five sub-catchments (ZJ, HK, FX, HS and PX) during the study period.

245 the stable isotopes of river water and precipitation exhibited similar trends, with depletion during winter and summer and enrichment during autumn and spring (Figure 2b-f and Table 2). The isotopic content of river water showed greater variability during the high flow period of summer compared to other seasons (Table 2). There was remarkable spatial variability of δD values in river waters across the study area (Figure 2, Table 2). River water δD values in the FX catchment showed the largest range of variations from -66.43 ‰ to -18.02 ‰ with a mean of -36.78±6.24 ‰ (Figure 1). In contrast, the HS exhibited the
250 smallest range of δD variation from -53.06 ‰ to -35.85 ‰ with a mean of -35.85 ±4.34 ‰. Moreover, the isotopic values in river water tend to be more negative in the east compared to the west. Specifically, ZJ exhibits the highest mean δ^{18}O and δD values (δ^{18}O: -5.31 ‰ and δD: -32.62 ‰), while PX has the lowest mean δ^{18}O and δD values (δ^{18}O: -7.77 ‰ and δD: -41.84 ‰).

The slope of the local meteoric water line (LMWL) in the study area (δD=7.73 δ^{18}O+13.03, n=268, R^2 = 0.95, p < 0.001)
255 was similar to the Global Meteoric Water Line (GMWL: δD = 8δ^{18}O+10, Figure 2). In contrast, the slope and intercept of linear regression line between δD and δ^{18}O for all river waters (EWL: δD = 4.41δ^{18}O – 9.32, n= 485, R^2 = 0.72, p < 0.001) were considerably lower than those of GMWL and LMWL of precipitation (Figure 4a). The slopes and intercepts of EWL for river waters ranged from 3.78 to 6.6, and from -13.12 ‰ to 4.5 ‰ in five sub-catchments, respectively (Figure 3b). The

Table 2. Seasonal variations (mean±SD) of $\delta^{18}O$, δD, and d-excess in precipitation and river waters from five sub-catchments throughout the entire study period.

Seasons	Isotopes	Precipitation	HK	FX	ZJ	PX	HS
Winter(Dec.-Feb.)	$\delta^{18}O$ (‰)	-6.5±3	-6.9±1.1	-6.5±1	-5.7±0.5	-7.7±0.9	-6.4±0.4
Winter(Dec.-Feb.)	δD (‰)	-31.1±27	-40.1±5	-38.2±2	-35±2	-41.9±4	-35.7±3
Winter(Dec.-Feb.)	d-excess (‰)	21.1±7	15.6±5.8	14.2±5	10.6±2	19.7±4.5	15.5±2.7
Spring(Mar.-May.)	$\delta^{18}O$ (‰)	-3.6±2	-6.9±1	-5.9±1	-5.1±0.5	-7.3±0.7	-6.4±0.8
Spring(Mar.-May.)	δD (‰)	-13.8±20	-36.9±4	-33±6	-29.1±4	-39.3±3	-34.7±5
Spring(Mar.-May.)	d-excess (‰)	15.5±6	18±4.6	14.4±5	12.1±3.4	19.3±4.2	16.6±3
Summer(Jun.-Aug.)	$\delta^{18}O$ (‰)	-6.2±3	-7±1.4	-6±1	-5.3±1.4	-8.2±1.5	-6.6±0.5
Summer(Jun.-Aug.)	δD (‰)	-31.6±29	-39.6±7.5	-38.6±8	-34.2±12	-45.5±8	-37.5±5
Summer(Jun.-Aug.)	d-excess (‰)	7.6±5	16.1±4.7	9.4±3	8.5±3.9	20.6±4.9	15.4±2.5
Autumn(Sep-Nov)	$\delta^{18}O$ (‰)	-5.6±3	-6±0.7	-5.8±1	-5±0.8	-7.9±0.7	-6.2±0.5
Autumn(Sep-Nov)	δD (‰)	-28±26	-37.2±3	-36.5±3	-31.3±3	-41.4±3.6	-35.7±2
Autumn(Sep-Nov)	d-excess (‰)	14.7±8	10.5±3	10±6	8.9±4.6	21.9±3.4	14.2±3.6

largest slope and intercept of EWL were observed in ZJ catchment. Moreover, the d-excess of precipitation exhibited significant

260 temporal heterogeneity, ranging from -15.09 ‰ to 35.87 ‰ with an arithmetic mean of 14.57 ‰. The d-excess values were lowest in summer and highest in winter. However, the mean d-excess values (mean ±1SD) of river water in PX (20.34 ± 4.29 ‰), HK (14.99 ± 5.42 ‰), and HS (15.43 ± 3.03 ‰) watershed were greater than precipitation d-excess value, respectively (Table 2). The mean d-excess values of river in ZJ (9.87 ± 3.81 ‰) and FX (11.83 ± 6.03 ‰) are lower compared with mean precipitation d-excess. In terms of the correlation between δ^{18}O and d-excess, river water in HK watershed exhibits

265 the significant relationship (p<0.01), followed by PX and FX, while HS and ZJ show a weaker correlation between δ^{18}O and d-excess (Figure 3c).
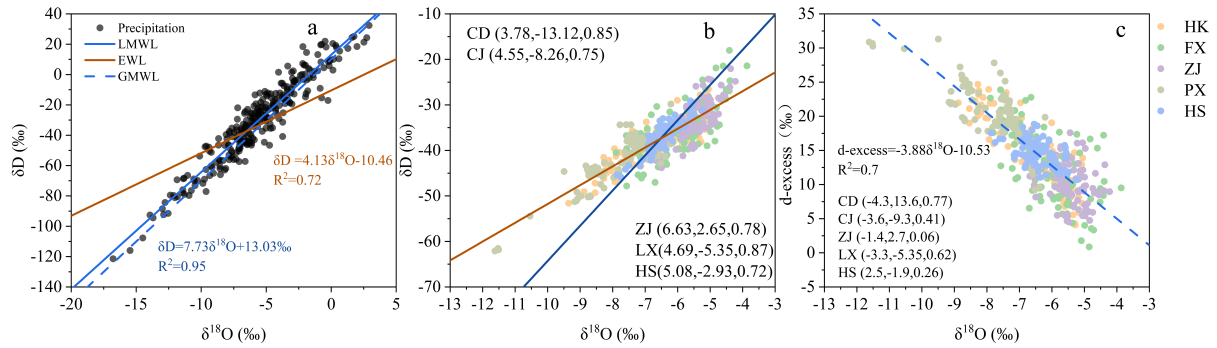
Figure 3. Linear regression relationships between δD and δ^{18}O for (a) precipitation, (b) river water and (c) plot of d-excess versus δ^{18}O for river water. Blue line represents the local meteoric water line (LMWL) in (a); Blue lines represent regression lines for surface water samples in (b); blue dot-dash line represents the Global Meteoric Water Line (GMWL), expressed as δD=8δ^{18}O+10; The first, second, and third positions within the parentheses represent the slope, intercept, and R-squared value of five specific sub-catchments (HK, FX, ZJ, PX, and HS), respectively.

3.2 Young water fraction (F_{yw}) and new water fraction (F_{new}) estimation

As shown in Figure 4, the δD in precipitation and river water exhibited remarkable periodicity; its seasonal variation trend can be well fitted with a sine-wave curve. Notably, the curve fit was least satisfactory in the ZJ catchment (R^2=0.18) and most effective in the HK catchment (R^2=0.41). The sine regression models of both precipitation and river water were statistically significant ($p < 0.001$). Precipitation sinusoidal waves peaked in March and reached their lowest points in September, exhibiting the most significant seasonal fluctuation with the highest amplitude. Meanwhile, sinusoidal waves in river water from different catchments were dampened to varying degrees compared to precipitation. Figure 4 illustrated the fitted phase shift (ϕ) of δD in precipitation and river water. The fitted ϕ values for river water are consistently larger than that of precipitation, indicating a time lag between the signal of river water and precipitation input. The amplitude values in five sub-catchments range from 1.2 to 3.7, which is associated with the estimated τ_{yw} and F_{yw} (Table 3). The range of F_{yw} and τ_{yw} spans from 0.07 to 0.21, and from 0.1 to 0.26 years, respectively. Among them, the HS catchment has the lowest Fyw, while the HK catchment has the highest F_{yw}. The transit-time distribution of river water is determined by the shape factor (α), which ranges from 0.06 to 1.38 (Table 3).
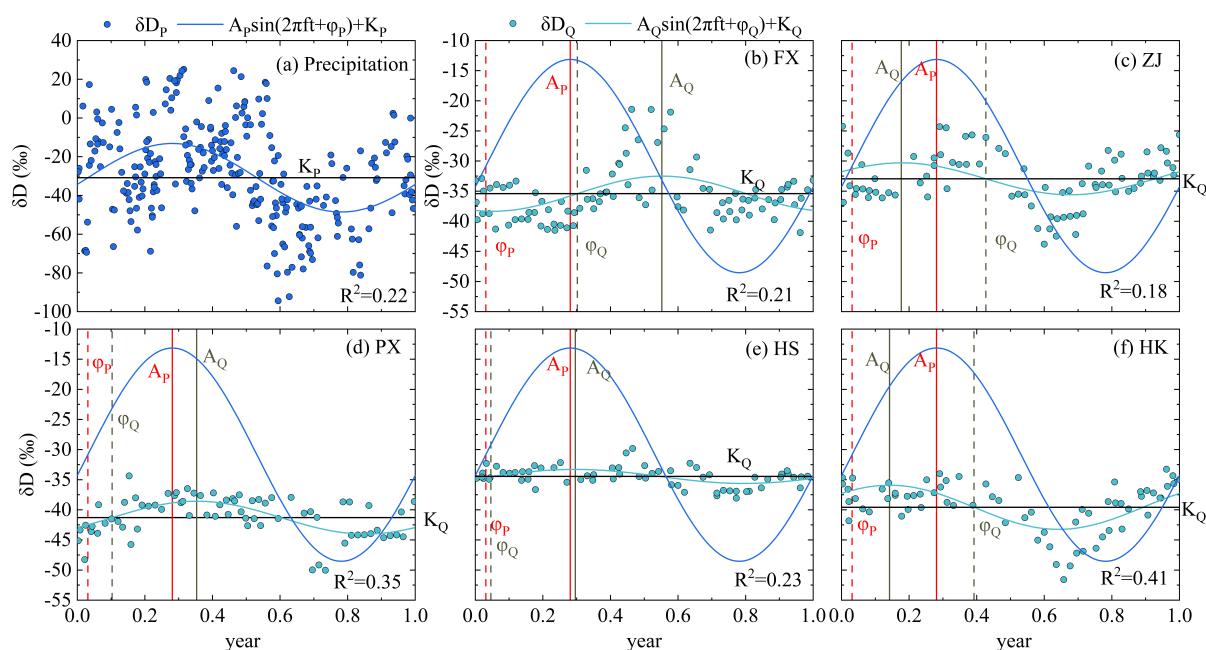
Figure 4. Annual-cycle-normalized sinusoidal cycles of both precipitation (a) and river waters (b-f) fitted by δD data for five sub-catchments. A_p and A_Q, ϕ_p and ϕ_Q, K_P and K_Q represent the amplitudes, phase shifts and vertical shifts of sine-wave curve fitted by precipitation (subscript p) and river water (subscript Q), respectively.

Table 3. Summary of all the relevant parameters estimated for five subcatchments.

subcatchments	$A_Q \pm$ SE	$\phi_Q \pm$ SE	$F_{yw\_all} \pm$ SE	$\alpha \pm$ SE	$\tau_{yw} \pm$ SE (yr)
HS	1.2±0.2	-0.1±0.1	0.07±0.01	0.06±1.3	0.1±0.07
HK	3.7±0.3	0.7±0.1	0.21±0.02	0.58±2.7	0.15±0.04
ZJ	2.7±0.4	0.5±0.1	0.15±0.02	0.4±2.2	0.14±0.06
FX	2.9±0.1	1.2±0.1	0.17±0.02	1.03±2.9	0.19±0.12
PX	2.7±0.2	0.3±0.1	0.15±0.02	1.38±1.24	0.2±0.07

Notes: A_Q, ϕ_Q represent the amplitudes, phase shifts of sine-wave curve fitted by river water.

280   Anticipating variability in F_{yw} over time, Figure 5 shows the distribution of unweighted (F_{yw_60}) and flow-weighted ($F^*_{yw\_60}$) young water fraction values, using a 1-year window shifted at 1-month intervals. Notably, the uncertainty associated with the time-variable results was greater than that of the F_{yw_all} results (Figure 5 and Table 3). Moreover, both $F^*_{yw\_60}$ results and F_{yw_60} results closely mirrored the F_{yw_all} values, with HK catchment registering the highest Fyw and the HS catchment the lowest F_{yw}. Generally, our data indicate low and tightly distributed unweighted F_{yw} but higher and more broadly distributed

285   flow-weighted F_{yw}. Specifically, river water in the HS and HK watersheds showed a relatively tight distribution of unweighted

and flow-weighted F_{yw}, while the ZJ catchment demonstrated a relatively broader distribution of unweighted and flow-weighted F_{yw} Additionally, the FX and PX catchments displayed the highest temporal variability in $F^*_{yw\_60}$ and F_{yw_60}.
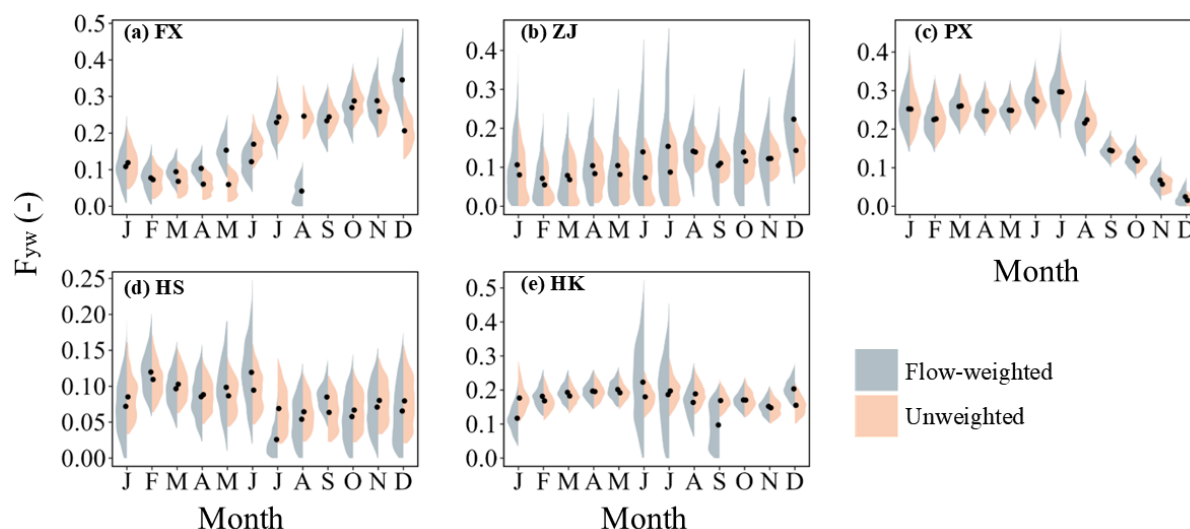
Figure 5. Flow-weighted $F^*_{yw\_60}$ (blue) and unweighted F_{yw_60} (orange) of five subcatchments. The month in the figure represents the month at the beginning of the one-year time window, the shape represents the probability density of young water fraction, the black line represents the 95% confidence interval and red line represents mean value.

Table 4 shows that the range of F_{new} based on d-excess calculation varied from 0.09 to 0.27, with a high correlation coefficient with F_{yw_all} in the study area (r=0.69, p<0.01). Among these values, the HS catchment has the lowest F_{new}, while the FX catchment has the highest F_{new}. In contrast, F_{new} based on δD calculation ranged from 0.004 to 0.03, and its Pearson's correlation coefficient (0.007 to 0.15) was significantly lower compared to that calculated from d-excess (Table 4).

Table 4. Spatial variation of F_{new} based on the calculation of d-excess and δD

Catchments	$F_{new\_d-excess}$	Pearson's r	$F_{new\_\delta D}$	Pearson's r
ZJ	0.23	0.26	0.004	0.02
PX	0.22	0.44	0.006	0.07
HK	0.19	0.47	0.006	0.007
FX	0.27	0.4	0.03	0.15
HS	0.09	0.3	0.015	0.13

4 Discussion

4.1 Spatial-temporal variations of stable isotopes in river water

Stable water isotopes serve as robust recorders to identify crucial catchment processes such as evaporation, transpiration,
295 recycling, and mixing, and to assess catchment water balance (Wu et al., 2021). In this study, river water isotopes exhibited
high spatial heterogeneity from west to east (Figure 3 and Table 2). This heterogeneity may be explained by the contrasting
local surface evaporation, or different recharge sources in various catchments of river water (Li et al., 2020; Wang et al., 2022;
Wu et al., 2017). The isotopic data of river water in the study area were scattered along both sides of the LMWL (Figure 3),
indicating that river water may be of meteoric origin (Bugna et al., 2020). Furthermore, the $\delta^{18}O$ and δD data point distribution
300 of samples from a single small catchment was relatively concentrated (Figure 3b), indicating that all the river water in each
catchment originates from the same water source or undergoes similar hydrological processes. The variability in isotopic
composition of precipitation was larger than that of river water, illustrating that the damping of the precipitation signatures due
to mixing and dispersion within the subsurface. Besides, some overlap of the $\delta^{18}O$ and δD data points occurs for two closely
adjacent catchments, which can be attributed to the high similarity in their climatic and geographical features(Bhat et al., 2022).
305 However, the slope and intercept of the EWL were quite different from those of the LMWL. This discrepancy suggests that the
linear regression between δD and $\delta^{18}O$ in surface waters reflects, to some extent, the local evaporation condition (Shi et al.,
2019). Therefore, river water in the study area experienced a higher degree of evaporation, with river water in the ZJ catchment
being the least affected.

Precipitation d-excess is strongly influenced by the relative humidity of the moisture source, which changes with varying
310 surface water temperatures and subsequent alterations in evaporation rates (Zhengyu and Matthew, 2021). This is the main rea-
son for the time variability of precipitation d-excess (Table 2). The lower d-excess in summer precipitation may be attributed
to higher summer temperatures leading to increased secondary evaporation of raindrops(Natali et al., 2022). In addition, be-
cause of kinetic fractionation processes, evaporation preferentially removes the light isotopes and leaves heavy isotopes in the
residue liquid phase, resulting in a prominent isotopic enrichment of heavy isotopes in the remaining waters (Mao et al., 2021).
315 Consequently, river water samples that experienced evaporation were mainly distributed along the evaporation line (Figure
3b), which has a lower slope (<8). Moreover, the d-excess values of the remaining water will decrease progressively, showing
a negative correlation with the $\delta^{18}O$ values (Soldatova et al., 2016; Wu et al., 2017). As shown in Figure 3c, the correlation
between d-excess and $\delta^{18}O$ in the ZJ and HS catchments is poor. On the contrary, d-excess of river water in the HK, FX, and
PX catchments has a good correlation with $\delta^{18}O$ values, indicating that river waters in the HK, FX, and PX catchments are
320 significantly affected by evaporative fractionation.

4.2 Water age dynamics and its comparison of water age using different approaches

In this study, the isotopic compositions from adjacent sub-catchments show differences, and the goodness of fit of re-
gression curves varies greatly, with R^2 values ranging from 0.18 to 0.41 (Figure 4). These differences reflect the seasonal
variations caused by the dominant runoff flow path and storage capacity within the catchment (Herms et al., 2019). During wet

325 conditions, once these flow paths become activated, pre-event and event water can be rapidly routed to the catchment outlet, temporarily masking seasonal variations in streamflow isotope data (Stockinger et al., 2016; Zhang et al., 2021). Additionally, as the isotopic composition of groundwater is generally constant, the amplitude of isotopes in river water will be weakened when groundwater feeds river water (Murgulet et al., 2016). These combined factors contribute significantly to the spatial heterogeneity of F_{yw} and τ_{yw} within the catchment. Besides, Table 2 lists the relatively low uncertainty ranges of F_{yw} and τ_{yw},

330 indicating that the sampling period and high-sampling interval of river water (2 years and 7-day intervals) were appropriate for this study. The average F_{yw} and τ_{yw} values are close to the global assessment by Jasechko et al. (2016), with F_{yw} estimated to be between 4% and 53%, and a τ_{yw} of streamflow of 3 months. Recent studies calculated the river water F_{yw} for several subtropical catchments, resulting in values of 21% (Xiao et al., 2022), 14% 35% (Hu et al., 2020), 31% (Zhang et al., 2020), and 29% (Gou et al., 2022), which are consistent with the results of the study. Estimated F_{yw} contributions suggest that the majority (on

335 average 80%) of total streamflow may originate from slow subsurface lateral flow and groundwater. Besides, the shape factor (α) values for HS, HK, and ZJ river water were less than 1, indicating a relatively rapid response to the input signal, while the α values for FX and PX were greater than 1.0, indicating a more attenuated response. Except in the HS watershed where the fitted ϕ value is similar between precipitation and river water, the ϕ values of river water are all larger than those of precipitation. This indicates that a time lag exists between river water and precipitation. This lag occurs because precipitation contributes to

340 the river not only through direct flow but also through delayed inputs like interflow and groundwater flow, causing a phase time lag (Xia et al., 2023).

Fitting a single sine wave to multi-year data oversimplifies the inter-annual variability in meteoric and streamflow isotope data, while annual sine waves better capture this variability(Stockinger et al., 2019). Considering inter-annual amplitude differences, our data indicate low and tightly distributed unweighted F_{yw} in the HS catchment, but higher and equally tightly

345 distributed unweighted F_{yw} in the HK catchment. These results could be attributed to both catchments having higher storage capacity, resulting in less noticeable interannual variability in F_{yw}. Additionally, the dominance of fast flow paths in HK catchment aids in the generation of young water. Similarly, the highest temporal variability in unweighted F_{yw} of the FX and PX catchments can be ascribed to different runoff flow paths activated at interannual scales. Flow-weighting is known to have an effect on F_{yw} at sites with relatively large variations in discharge (von Freyberg et al., 2018). In this study, flow-weighted F_{yw}

350 are generally higher than the unweighted F_{yw}, but differences between them are not significant (Figure 5). Trinh et al (2020) found that the flow-weighted and unweighted F_{yw} in the Day River Catchment in northern Vietnam were similar, characterized by 51±19% and 52±36%, respectively. This may reflect the similarity in water age distribution between dry and wet periods in tropical and subtropical catchments. As shown in (Gou et al., 2022), despite differences in the age distribution of streamflow between the winter and summer monsoon periods, there is a consistent preference for the preferential release of young water.

355 Additionally, the distribution of flowweighted F_{yw} is broader than that of unweighted F_{yw} in the HS and HK catchments. This finding suggests that flow-weighed F_{yw} can take the impact of anomalous events into account, therefore capturing some important hydrological characteristics of the catchment (Trinh et al., 2020). Overall, there's a higher temporal variability in F_{yw} compared to its spatial variability. This indicates that while intrinsic catchment characteristics have some impact on F_{yw}, it is likely primarily controlled by meteorological factors.

While the assumption of collinear behavior between $\delta^{18}O$ and δD is common, Bansah and Ali (2019) have suggested that inconsistencies in the F_{yw} calculations can arise when using $\delta^{18}O$ and δD (Bansah and Ali, 2019). This is not surprising, given that isotopic fractionation effects are known to affect δD more significantly. In this study, regression analysis revealed that using d-excess provided a better fit than using δD (Table 4). The differences in results generated by the two fingerprints are likely attributable to strong evaporative processes (Figure 3c). A similar study found that d-excess is a reliable tracer for tracing recharged water, especially resulting from evaporation during infiltration, which imparts a characteristic isotopic trend reflecting local climatic conditions (Wu et al., 2017). Therefore, it is plausible that the values of F_{new} calculated using d-excess above the values based on δD, potentially represent the new water that experienced evaporative fractionation loss within 1 to 2 weeks period. Besides, evaporation clearly has a greater impact on new water compared to old water (Table 4), possibly because the evaporation process slowed down the mixing of new water in the topsoil and old water in the lower layer (Chen et al., 2024).

4.3   Time-variable F_{yw} and F_{new} drivers

In traditional statistical frameworks, the inclusion of additional contributing drivers typically correlates with enhanced predictability and accuracy. Therefore, this study considered various potential predictors to identify those that significantly affect the riverine time-variable F_{yw}. The striking difference between the more powerful and less powerful predictors is illustrated in Figure 6. Meteorological variables such as potential evapotranspiration (PET) and precipitation (P) were among the most important drivers in each model, explaining the strong temporal heterogeneity observed in F_{yw}, as climate not only influences the underlying surface landscape but also fundamentally governs existing underlying surface characteristics, which in turn alters watershed hydrological characteristics. However, there is no significant relationship between the precipitation and F_{yw}. Part of the reason may be owing to limited data availability for stream water-age analysis, but it is more likely that this reveals the indirect influence of precipitation and evapotranspiration on the young water generation. Furthermore, we employed Shapley Additive Explanations (SHAP) to quantify the contributions of different driving factors to the young and new water fraction. The results highlight the influence of watershed attributes (e.g., river area, slope, and cropland proportion), and the correlations reflected by SHAP values are consistent with the Pearson correlation results (Figure 6a). Although meteorological factors (e.g., precipitation and evapotranspiration) are important drivers, their correlations with the young and new water fraction are not statistically significant, but river area (RA) demonstrates strong importance in both the RF and SHAP models. This reflects the integration power of the riparian zone, which efficiently mix waters with different water ages, potentially weakening the direct influence of precipitation on stream new and young water. Furthermore, percentage of sand in soil had the weakest predictive power in all cases.
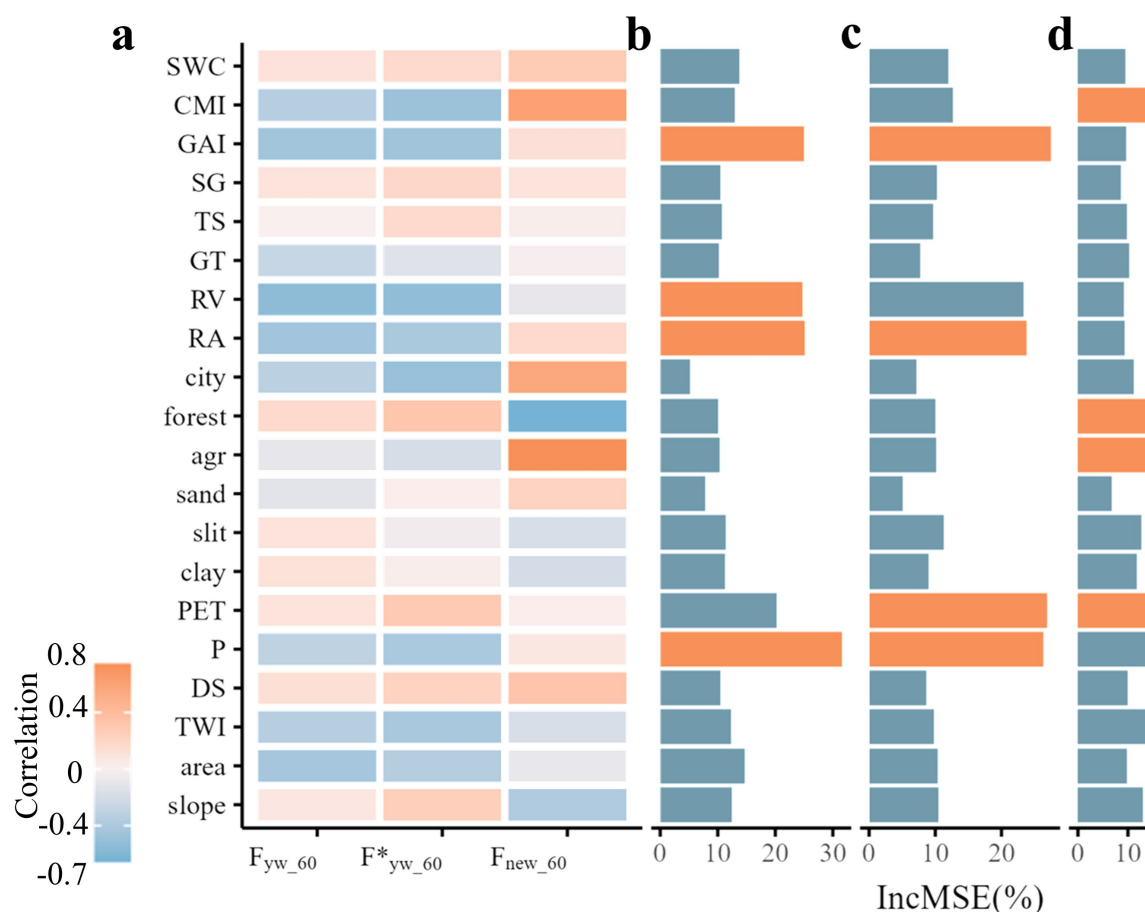
Figure 6. Heatmap of correlations of F_{yw_60}, $F^*_{yw\_60}$ and F_{new_60} with potential drivers (a) and the corresponding driver contributions (b, c, and d). The horizontal bars illustrate the mean variable importance for predicted drivers of F_{yw_60}, $F^*_{yw\_60}$ and F_{new_60} obtained in 1,000 random forest runs (b, c, and d), with orange bars highlighting the top four most significant drivers. Predicted drivers included in the analysis are mean annual potential evapotranspiration (PET), soil water content (SWC), Global Aridity Index (GAI), river volume (RV), CMI (Climate Moisture Index), River Area (RA), percentage of agriculture (agr), Discharge density(DS), catchment area (area), percentage of silt in soil (slit), Topographic Wetness Index (TWI), percentage of clay in soil (clay), Stream Gradient(SG), GTD (Groundwater Table Depth), slope (slope), percentage of sand in soil (sand), mean annual precipitation (P), percentage of urban areas (city), percentage of forest (forest).

The prediction results for the drivers of F_{yw} and F^*_{yw} show consistent performance between the RF and SHAP models,
390   both emphasizing the importance of RA, further supporting the assumption that the watershed tends to release young water in both wet and dry seasons due to the regulatory function of the riparian zones. Unlike the drivers of F_{yw}, the drivers of F_{new} place greater emphasis on the importance of land use types, as indicated by the prediction results of both the RF and SHAP models. Specifically, the proportion of agricultural area shows a significant positive correlation with F_{new} (Figs. 6 and 7) likely due to the extensive conversion of riparian zones into cropland near the watershed outlet. For example, plough pan development

395   resulting from agricultural activities decreases the likelihood of deep infiltration (Trinh et al., 2020). This may have contributed to the higher uncertainty in F_{yw} in the ZJ catchment, which has a relatively high proportion of cropland (Figure 1). Additionally, the weaker influence of RA suggests that watershed convergence has a limited impact on F_{new}. In contrast to previous studies (Jasechko et al., 2016; Ye et al., 2022), the influence of basin slope on F_{yw} appears to be less significant, possibly due to the relatively low slope of our study area. Previous research has emphasized that steeper terrain in mountainous catchments results

400   in the prevalence of deeper infiltration flow paths, thereby reducing F_{yw} (Jasechko et al., 2016).
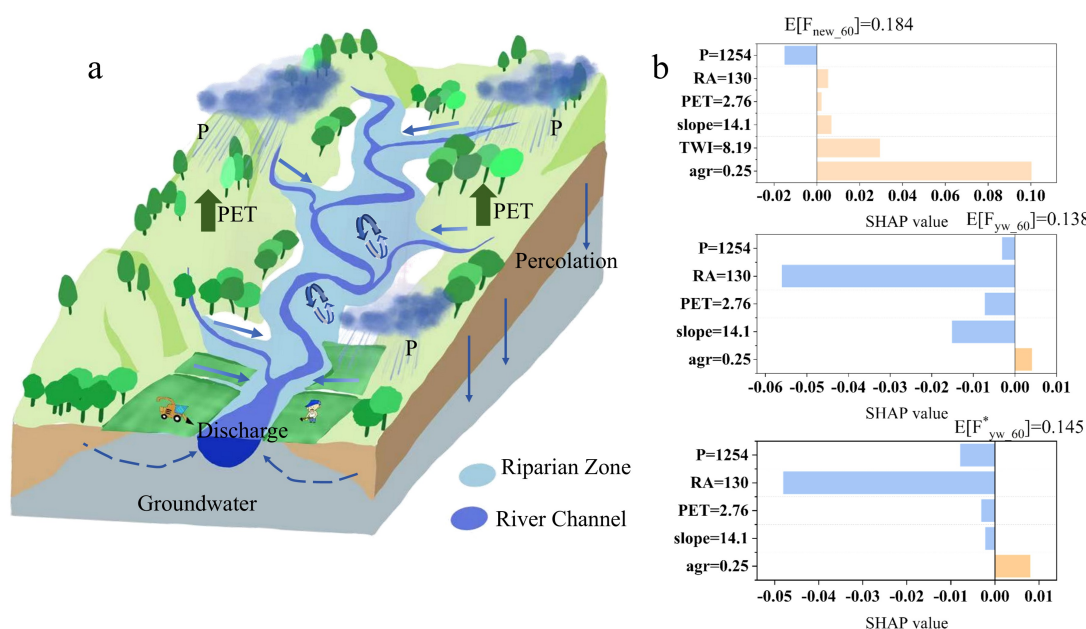
Figure 7. Conceptual diagram (a) and the contribution of the most important variables in predicting young and new water fraction (b), as estimated by the SHAP values (only driving factors with significant impacts were displayed, while those with lower SHAP values were not shown).

5   Conclusions

     In this study, high-resolution time series of stable isotope data were firstly collected to estimate spatiotemporal variations of young and new water fraction in five headwater sub-catchments from the upper reaches of Xiu River, located within the Poyang Lake catchment of South-Central China using the sine-wave approach and mixing end-members model. The δD

405   and $\delta^{18}O$ of river water was mainly scattered around the LMWL ($\delta D=7.73\delta^{18}O+13.03$, $R^2 =0.95$, p<0.001), indicating that river water primarily originated from atmospheric precipitation. Additionally, both the slope and intercept of EWL ($\delta D = 4.41\delta^{18}O–9.32$, $R^2 =0.72$, p < 0.001) were lower than those of the LMWL. Furthermore, river water was characterized by a lower riverine F_{yw}, which exhibited high spatiotemporal heterogeneity. The interplay of various controls on time-variable F_{yw}

and F_{new} was confirmed in a random forest analysis, revealing that precipitation (25.48±5.41%) and potential evapotranspira-
tion (27.84±6.62%) were the main drivers that explained the time-variable F_{yw} and F_{new} in the study area. Precipitation serves
as the source of young and new water, while evapotranspiration reduces the amount of water along flow paths, thus affecting
both young and new water fraction. Spatially, different land use types were identified as the primary drivers of the significant
spatial heterogeneity in F_{new} and F_{yw}. These land use types determined the generation of young and new water by altering the
proportion of different flow paths and the amount of undersurface water storage, with a greater impact on water in faster flow
paths. Furthermore, the SHAP analysis revealed a negative correlation between river area and F_{yw}, and a positive correlation
between cultivated land proportion and F_{new}, which suggested that riparian zones regulated and mix young water, while human
conversion of these zones into agricultural land could weaken this impact. This study offers novel insights into the evolution of
riverine water age, enhancing our understanding of catchment-scale hydrological processes and guiding the management and
protection of water resources in subtropical headwater regions.

Code and data availability. The data and code that support the findings of this study are available from the corresponding author upon
reasonable request.

Author contributions. Conceptualization: KL. Methodology: KL and HW. Formal analysis: KL and HW. Data curation: HF, RL, and MD.
Writing-original draft: KL and HW. Writing-review and editing: HW, HF, RL, MD, JL, CF, CZ, GS, RR, and XX. Visualization: KL.
Supervision: KL, HW and HF.

Competing interests. The contact author has declared that none of the authors has any competing interests.

Acknowledgements. This work was supported by National Natural Science Foundation of China, China (U2240219, 42201105, and 42071145),
Qinghai University Research Ability Enhancement Project (2025KTST03), and Science and Technology Planning Project of NIGLAS (NI-
GLAS2022GS10).

References

430 Bagheri, R., Bagheri, F., Karami, G.H., Jafari, H. (2019). Chemo-isotopes (^{18}O & ^{2}H) signatures and HYSPLIT model application: Clues to the atmospheric moisture and air mass origins. *Atmospheric Environment*, 209, 116892.

Bansah, S., Ali, G. (2019). Streamwater ages in nested, seasonally cold Canadian watersheds. *Hydrological Processes*, 33(4), 495-511.

Benettin, P., Fovet, O., Li, L. (2020). Nitrate removal and young stream water fractions at the catchment scale. *Hydrological Processes*, 34(12), 2725-2738.

435 Bhat, M.A., Zhong, J., Dar, T., Kumar, A., Li, S.-L. (2022). Spatial distribution of stable isotopes in surface water on the upper Indus River basin (UIRB): Implications for moisture source and paleoelevation reconstruction. *Applied Geochemistry*, 136, 105137.

Brantley, S.L., et al. (2017). Reviews and syntheses: on the roles trees play in building and plumbing the critical zone. *Biogeosciences*, 14(1), 1-41.

Bugna, G.C., Grace, J.M., Hsieh, Y.-P. (2020). Sensitivity of using stable water isotopic tracers to study the hydrology of isolated wetlands
440 in North Florida. *Journal of Hydrology*, 586, 124321.

Burt, E.I., Goldsmith, G.R., Cruz-de Hoyos, R.M., Ccahuana Quispe, A.J., West, A.J. (2023). The seasonal origins and ages of water provisioning streams and trees in a tropical montane cloud forest. *Hydrology and Earth System Sciences*, 27(22), 4173-4186.

Chen, X., et al. (2024). Effects of soil heterogeneity and preferential flow on the water flow and isotope transport in an experimental hillslope. *Science of The Total Environment*, 917, 170548.

445 Clow, D.W., Mast, M.A., Sickman, J.O. (2018). Linking transit times to catchment sensitivity to atmospheric deposition of acidity and nitrogen in mountains of the western United States. *Hydrological Processes*, 32(16), 2456-2470.

Cotton, J., et al. (2018). A bioavailable strontium isoscape for Western Europe: A machine learning approach. *Plos One*, 13(5), e0197386.

Craig, H. (1961). Isotopic Variations in Meteoric Waters. *Science*, 133(3465), 1702-1703.

Erdélyi, D., Kern, Z., Nyitrai, T., Hatvani, I.G. (2023). Predicting the spatial distribution of stable isotopes in precipitation using a machine
450 learning approach: a comparative assessment of random forest variants. *GEM - International Journal on Geomathematics*, 14(1), 14.

Gallart, F., et al. (2020). Investigating young water fractions in a small Mediterranean mountain catchment: Both precipitation forcing and sampling frequency matter. *Hydrological Processes*, 34(17), 3618-3634.

Gentile, A., et al. (2023). Towards a conceptualization of the hydrological processes behind changes of young water fraction with elevation: a focus on mountainous alpine catchments. *Hydrology and Earth System Sciences*, 27(12), 2301-2323.

455 Gou, J., et al. (2022). Seasonal variation of transit time distribution and associated hydrological processes in a Moso bamboo watershed under the East Asian monsoon climate. *Journal of Hydrology*, 2022, 128912.

Guan, Y., et al. (2022). Tracing anomalies in moisture recycling and transport to two record-breaking droughts over the Mid-to-Lower Reaches of the Yangtze River. *Journal of Hydrology*, 2022, 127787.

Harman, C. J. (2015). Time-variable transit time distributions and transport: Theory and application to storage-dependent transport of chloride
460 in a watershed. *Water Resources Research*, 51(1), 1-30.

Herms, I., et al. (2019). Contribution of isotopic research techniques to characterize high-mountain-Mediterranean karst aquifers: The Port del Comte (Eastern Pyrenees) aquifer. *Science of The Total Environment*, 656, 209-230.

Hu, M., Zhang, Y., Wu, K., Shen, H., Yao, M., Dahlgren, R. A., & Chen, D. (2020). Assessment of streamflow components and hydrologic transit times using stable isotopes of oxygen and hydrogen in waters of a subtropical watershed in eastern China. *Journal of Hydrology*,
465 589, 125363.

Ide, K., et al. (2020). Changes of groundwater flow systems after the 2016 Mw 7.0 Kumamoto earthquake deduced by stable isotopic and CFC-12 compositions of natural springs. *Journal of Hydrology*, 583, 124551.

Jasechko, S., et al. (2016). Substantial proportion of global streamflow less than three months old. *Nature Geoscience*, 9(2), 126-129.

Kim, M., et al. (2016). Transit time distributions and StorAge Selection functions in a sloping soil lysimeter with time-varying flow paths: Direct observation of internal and external transport variability. *Water Resources Research*, 52(9), 7105-7129.

Kirchner, J. W. (2019). Quantifying new water fractions and transit time distributions using ensemble hydrograph separation: theory and benchmark tests. *Hydrology and Earth System Sciences*, 23(1), 303-349.

Li, C., et al. (2020). Seasonal variability of stable isotopes in the Changjiang (Yangtze) river water and its implications for natural climate and anthropogenic impacts. *Environmental Sciences Europe*, 32, 1-13.

Li, Y., et al. (2016). The influence of river-to-lake backflow on the hydrodynamics of a large floodplain lake system (Poyang Lake, China). *Hydrological Processes*, 31, 117-132.

Lutz, S. R., et al. (2018). Spatial Patterns of Water Age: Using Young Water Fractions to Improve the Characterization of Transit Times in Contrasting Catchments. *Water Resources Research*, 54(7), 4767-4784.

Mao, H., Wang, G., Shi, Z., Liao, F., & Xue, Y. (2021). Spatiotemporal Variation of Groundwater Recharge in the Lower Reaches of the Poyang Lake Basin, China: Insights From Stable Hydrogen and Oxygen Isotopes. *Journal of Geophysical Research: Atmospheres*, 126, e2020JD033760.

Morissette, O., et al. (2023). Limited evidence for species-specific sensitivity of temperature-dependent fractionation of oxygen stable isotope in biominerals: A meta-analysis. *Methods in Ecology and Evolution*, 14(5), 1719-1731.

Murad, A. A., & Mirghni, F. M. (2011). Isotopic variations of oxygen and hydrogen in groundwater of carbonate aquifer in an arid environment. *Arabian Journal of Geosciences*, 5, 1459-1468.

Murgulet, D., et al. (2016). Impact of hydrological alterations on river-groundwater exchange and water quality in a semi-arid area: Nueces River, Texas. *Science of the Total Environment*, 572, 595-607.

Natali, S., et al. (2022). Is the deuterium excess in precipitation a reliable tracer of moisture sources and water resources fate in the western Mediterranean? New insights from Apuan Alps (Italy). *Journal of Hydrology*, 614, 128497.

Shi, M., et al. (2019). Stable Isotope Composition in Surface Water in the Upper Yellow River in Northwest China. *Water*, 11(11), 967.

Shi, X., et al. (2023). Tree species richness and functional composition drive soil nitrification through ammonia-oxidizing archaea in subtropical forests. *Soil Biology and Biochemistry*, 187, 109211.

Soldatova, E. A., Sun, Z., & Guseva, N. V. (2016). Isotopic composition (δ^{18}O and δD) of the shallow groundwater in the Poyang Lake basin. *IOP Conference Series: Earth and Environmental Science*, 33(1), 012011.

Song, C., et al. (2017). Stable isotope variations of precipitation and streamflow reveal the young water fraction of a permafrost watershed. *Hydrological Processes*, 31(4), 935-947.

Speed, M., et al. (2011). Evolution of the spatial and temporal characteristics of the isotope hydrology of a montane river basin. *Hydrological Sciences Journal*, 56(3), 426-442.

Stockinger, M. P., et al. (2016). Tracer sampling frequency influences estimates of young water fraction and streamwater transit time distribution. *Journal of Hydrology*, 541, 952-964.

Stockinger, M. P., et al. (2019). Time variability and uncertainty in the fraction of young water in a small headwater catchment. *Hydrology and Earth System Sciences*, 23(10), 4333-4347.

Trinh, A. D., et al. (2020). Using stable isotopes to estimate young water fractions in a heavily regulated, tropical lowland river basin. *Hydrological Processes*, 34(22), 4239-4250.

Valdivielso, S., et al. (2020). Origin and Variability of Oxygen and Hydrogen Isotopic Composition of Precipitation in the Central Andes: a Review. *Journal of Hydrology*, 587, 124889.

von Freyberg, J., et al. (2018). Sensitivity of young water fractions to hydro-climatic forcing and landscape properties across 22 Swiss catchments. *Hydrology and Earth System Sciences*, 22(7), 3841-3861.

Wang, L., et al. (2022). Water sources and recharge mechanisms of the Yarlung Zangbo River in the Tibetan Plateau: Constraints from hydrogen and oxygen stable isotopes. *Journal of Hydrology*, 614, 128585.

Wang, S., et al. (2023). Insights into the streamwater age in the headwater catchments covered by glaciers and permafrost, Central Tibetan Plateau. *Science of The Total Environment*, 866, 161337.

Wu, H., et al. (2021). Stable isotope signatures of river and lake water from Poyang Lake, China: Implications for river–lake interactions. *Journal of Hydrology*, 592, 125619.

Wu, X., et al. (2017). Origin of water in the Badain Jaran Desert, China: new insight from isotopes. *Hydrology and Earth System Sciences*, 21(9), 4419-4431.

Xia, C., et al. (2023). Stable isotopes reveal the surface water-groundwater interaction and variation in young water fraction in an urbanized river zone. *Urban Climate*, 51, 101641.

Xiao, Dacheng, Brantley, Susan L., & Li, Li (2021). Vertical Connectivity Regulates Water Transit Time and Chemical Weathering at the Hillslope Scale. *Water Resources Research*, 57(2), e2020WR029207.

Xiao, Xiong, Zhang, Xinping, Wu, Huawu, Zhang, Cicheng, & Han, Longfei (2022). Stable isotopes of surface water and groundwater in a typical subtropical basin in south-central China: Insights into the young water fraction and its seasonal origin. *Hydrological Processes*, 36(11), e14574.

Ye, Sheng, Liu, Lin, Chen, Xiuxiu, Li, Peng, Xu, Guoce, & Ran, Qihua (2022). The Variability of Stable Water Isotopes and the Young Water Fraction in a Mountainous Catchment. *Clean - Soil Air Water*, 50(12).

Zhang, Qinghuan, Knowles, John F., Barnes, Rebecca T., Cowie, Rory M., Rock, Nathan, & Williams, Mark W. (2018). Surface and sub-surface water contributions to streamflow from a mesoscale watershed in complex mountain terrain. *Hydrological Processes*, 32(23), 3364-3381.

Zhang, Zhicai, Chen, Xi, Cheng, Qinbo, & Soulsby, Chris (2020). Characterising the variability of transit time distributions and young water fractions in karst catchments using flux tracking. *Hydrological Processes*, 34(24), 5127-5143.

Zhicai Zhang, Xi Chen, Qinbo Cheng, & Chris Soulsby (2021). Using StorAge Selection (SAS) functions to understand flow paths and age distributions in contrasting karst groundwater systems. *Journal of Hydrology*, 599, 126785.

Zhengyu Xia and Matthew J. Winnick (2021). The competing effects of terrestrial evapotranspiration and raindrop re-evaporation on the deuterium excess of continental precipitation. *Earth and Planetary Science Letters*, 367, 117120.